



Contrasting aerosol mixing states at inland and coastal sites: an entropy-based metric for CCN activity

Jingye Ren^{1,2}, Wei Xu³, Ru-Jin Huang¹, Fang Zhang⁴, Ying Wang¹, Lu Chen⁵, Jurgita Ovadnevaite⁶, Darius Ceburnis⁶, Colin O'Dowd⁶, and Yele Sun⁷

¹State Key Laboratory of Loess Science, Institute of Earth Environment, Chinese Academy of Sciences, Xi'an, 710061, China

²Xi'an Institute for Innovative Earth Environment Research, Xi'an, 710061, China

³State Key Laboratory of Advanced Environmental Technology, Institute of Urban Environment, Chinese Academy of Sciences, Xiamen, 361021, China

⁴Shenzhen Key Laboratory of Organic Pollution Prevention and Control, School of Eco-Environment, Harbin Institute of Technology Shenzhen, Shenzhen, 518055, China

⁵School of Ocean and Geographic Science, Yancheng Teachers University, Yancheng, 224051, China

⁶School of Natural Sciences, Centre for Climate & Air Pollution Studies, Ryan Institute, University of Galway, University Road, Galway, Ireland

⁷State Key Laboratory of Atmospheric Boundary Layer Physics and Atmospheric Chemistry, Institute of Atmospheric Physics, Chinese Academy of Sciences, Beijing, 100029, China

Correspondence: Ru-Jin Huang (rujin.huang@ieecas.cn) and Fang Zhang (zhangfang2021@hit.edu.cn)

Received: 9 July 2025 – Discussion started: 15 July 2025

Revised: 12 January 2026 – Accepted: 24 January 2026 – Published: 27 February 2026

Abstract. Simplified assumptions of aerosol mixing states in modeling often introduce substantial uncertainties in estimating cloud condensation nuclei (CCN) concentrations (N_{CCN}) and their climatic impacts. This study systematically investigates the contrasting relationships between mixing states and CCN activity by combining field measurements of hygroscopicity with the algorithm of entropy at two inland and coastal sites. We show distinct seasonal variations of mixing state. In winter, externally-mixed particles dominated both sites, with comparable mixing state indices (χ) of 0.38 ± 0.12 and 0.39 ± 0.09 respectively for coastal and inland air. However, measurements in summer showed pronounced differences: aerosols in the coastal atmosphere exhibited a higher degree of internal mixing ($\chi = 0.69 \pm 0.19$), whereas inland χ values only increased moderately to 0.47 ± 0.12 . Aerosol mixing state is largely influenced by primary emissions and secondary formation process. Externally-mixed particles originate chiefly from anthropogenic emissions in inland or sea salt in coastal. With the aging process, particles become more internally-mixed as the enhanced fraction of more-hygroscopic mode. Both environments show the negative correlations between the critical diameter (D_{cri}) and χ but with distinct decrement rates for coastal vs. inland aerosols. Specially, D_{cri} exhibits heightened sensitivity to fluctuations in χ when $\chi < 0.5$. This offers a practical approach to estimate D_{cri} from χ when the particles are not highly aged. Further analysis reveals that N_{CCN} exhibits heightened sensitivity to fluctuations in χ at low values. These results underscore that mixing states exert different control over N_{CCN} in diverse environments and provide critical constraints for parameterizing fine aerosols CCN activity in models.

1 Introduction

Atmospheric cloud condensation nuclei (CCNs) are complex mixtures of organic and inorganic components. Their chemical and physical properties make quantifying aerosol-cloud interactions challenging (Liu et al., 2018; Rosenfeld et al., 2019; Xu et al., 2022, 2024; Virtanen et al., 2025), introducing uncertainties into climate effect assessments (Charlson et al., 1992; Shrivastava et al., 2017; IPCC, 2021; Chen et al., 2022a; Manavi et al., 2025). Accurate climate model predictions of aerosol impacts require understanding aerosol mixing states under different atmospheric conditions and their effects on CCN activity (Ching et al., 2016; Zheng et al., 2021a). Current models often oversimplify mixing states by assuming pure internal or external mixing (Winkler, 1973; Stevens and Dastoor, 2019; Riemer et al., 2019; Zheng et al., 2021b). This is problematic because mixing states directly determine particle hygroscopicity distribution and CCN estimates (Wang et al., 2010; Tao et al., 2024). For example, internal-mixed aerosol particles have unimodal hygroscopicity distribution, while the external-mixed particles are characterized by the bimodal/trimodal or partly overlapping structures (Spitieri et al., 2023; Liu et al., 2025). Such simplifications can lead to significant errors, e.g., Sotiropoulou et al. (2007) found that mixing state assumptions caused two-fold N_{CCN} estimation errors in global models.

Systematic observations across diverse environments are critical because aerosol mixing states exhibit pronounced spatial-temporal variations (Ye et al., 2018; Hughes et al., 2018; Liu et al., 2025). For example, continental and coastal regions present contrasting scenarios (Ramachandran and Srivastava, 2016). The continental areas are dominated by anthropogenic emissions, where aerosol aging is driven by industrial and traffic-related pollutants (Huang et al., 2014; Ren et al., 2023). Particles here undergo progressive internal mixing via photochemical process and heterogeneous reactions, altering their hygroscopic properties (Ervens et al., 2010; Tao et al., 2021). While the coastal regions feature dynamic interactions between marine aerosols (e.g., sea salt) and continental pollutants (Schill et al., 2015; Collins et al., 2013; Cheung et al., 2020). Seasonal shifts in air mass sources (e.g., marine vs. continental dominance) might create unique mixing state patterns (Xu et al., 2020, 2021a). For instance, summer photochemical aging and heterogeneous processes in coastal areas can enhance the degree of internal mixing, while winter often retains more external mixing due to the presence of the sea-salt particles with less-hygroscopic organic matter.

The continental aerosols influence regional cloud formation, while coastal aerosols may provide insights into the characteristics of marine aerosols in region. The properties of marine aerosols are significantly different from those of continental aerosols, and therefore have distinct climate feedback mechanisms (Bellouin et al., 2020; Xu et al., 2024; Liu et al., 2024). However, the current models lack regional-

specific mixing state parameters and usually assume uniform mixing in both environments. This could lead to large uncertainties in predicting CCN concentrations, highlighting the need for site-specific observations. For example, Ren et al. (2018) found that the impact of aerosol mixing state on CCN activation characteristics ranged from -34% to $+16\%$ in urban atmosphere. Comparison between a fully internal mixture assumption and using the mixing state index from the particle-resolved model, Ching et al. (2017) found the obvious overestimation in CCN concentration. Especially in the regions e.g., Amazon Basin, Central Africa and Indonesia, the particles appeared to be more external, errors in CCN concentration would increase up to 100% (Hughes et al., 2018). A detailed exploration of mixing state on CCN concentration in global scale was conducted by Zheng et al. (2021a), and the results showed that the mixing state varied spatially with more externally mixed over the North Atlantic Ocean, off the coasts of Southern Africa, and Australia. Thus, assuming particles with internally-mixed would introduce errors in CCN concentration of 50% – 100% .

Therefore, for quantifying the aerosol mixing state in the ambient atmosphere, we apply the algorithm of entropy proposed by Riemer and West (2013) to investigate the aerosol heterogeneity. This index has been applied to quantify the mixing state more reasonably both in field campaigns (Zhao et al., 2021; Yuan and Zhao, 2023) and model simulations (Ching et al., 2016; Zheng et al., 2021a). However, most studies focused on quantifying the particle heterogeneity in composition (Ching et al., 2019; Fierce et al., 2020; Zhao et al., 2021). Here we concentrated on evaluating the heterogeneity in aerosol hygroscopicity for sub-micron particles, which directly related to CCN budget. By refereeing to Yuan et al. (2023), the heterogeneity in hygroscopicity was investigated by combining in-situ measurements of probability distribution function of the hygroscopicity with the algorithm of entropy. Briefly, the mixing state index χ , is devised based on the concept of information entropy concerning the distribution of hygroscopicity across the aerosol population. It varies between 0 (external mixing completely) and 1 (internal mixing completely). By integrating inland and coastal measurements, this study will focus on addressing two key gaps, (1) how continental vs. marine-dominated environments shape aerosol mixing states and CCN activity; (2) whether χ -based CCN parameterizations show regional dependencies, providing critical constraints for climate models.

2 Data and methods

2.1 Field campaigns

The inland atmospheric measurements were conducted for two campaigns from 16 November to 6 December 2016 and 29 May to 13 June 2017 as a part of the Air Pollution and Human Health (APHH) project (Shi et al., 2019), at the Institute

of Atmospheric Physics, Chinese Academy of Sciences (IAP, 39.97° N, 116.37° E) in urban Beijing. The campaigns were complemented by the hygroscopicity and CCN observations and were conducive to provide information on the aerosol hygroscopicity affecting urban pollutions. This urban site exhibited highly variable aerosol populations dominated by local anthropogenic sources including vehicular, cooking emissions, and residential heating. Coastal measurements were performed at the Mace Head atmospheric research station (MHD, 53.33° N, 9.90° W) from 1 November 2009 to 30 January 2010, and summer periods from 11 to 31 August 2009 and July 2010, which located on the west coast of Ireland. Aerosol particles here experience alternating influences from polluted continental and clean marine atmospheres. The map of the sites was shown in Fig. 1. More details about the campaigns were given in Fan et al. (2020) and Xu et al. (2021a).

2.2 Instrumentation

2.2.1 Hygroscopicity measurements

The particle hygroscopicity at both sites was characterized using the humidified tandem differential mobility analyzer (HTDMA). The hygroscopic growth factor (Gf), defined as the ratio of the particle diameter at the fixed RH (90 %) and dry diameter set in this study for 40, 80, 110, 150, 200 nm at IAP and 35, 50, 75, 110 and 165 nm at MHD, respectively. The RH calibration with ammonium sulfate for HTDMA system was given in Fig. S1. The Gf probability density function (Gf-PDF) was derived using the TDMAinv algorithm (Gysel et al., 2009). The number fraction (NF) of near-hydrophobic mode (NH: $Gf \leq 1.21$), and more hygroscopic mode (MH: $Gf > 1.21$) in IAP site was referred from Chen et al. (2022b). It was integrated into three modes for the MHD site with the near-hydrophobic mode (NH: $1 < Gf < 1.3$), more hygroscopic mode (MH: $1.3 \leq Gf < 1.85$) and sea salt mode (SS: $Gf \geq 1.85$) for further examination (Xu et al., 2021a).

Here for each particle size, the hygroscopicity parameter κ can be subsequently calculated using κ -Köhler theory (Peters and Kreidenweis, 2007):

$$\kappa = \left(Gf^3 - 1 \right) \cdot \left[\frac{1}{RH} \exp \left(\frac{4\sigma_{s/a} M_w}{RT \rho_w D_d Gf} \right) - 1 \right] \quad (1)$$

where RH is the HTDMA relative humidity (90 % set in the instrument), $\sigma_{s/a}$ is the surface tension of pure water (0.072 J m^{-2}), M_w and ρ_w are the molecular weight and the density of pure water, R is the gas constant, and T is the absolute temperature, D_d is the droplet diameter.

Then, the κ -PDF is obtained and normalized as $\int_0^\infty c(\kappa) d\kappa = 1$, where $c(\kappa)$ is normalized as κ -PDF. Further it was used to calculate the particle population heterogeneity (Calculation seen in Sect. 2.3).

According to the κ -Köhler theory, the critical diameter (D_{cri}) corresponding to the supersaturation ratio can be ex-

pressed as:

$$D_{\text{cri}} = \sqrt[3]{\frac{4A^3}{27\kappa \ln^2 S}}, \quad A = \frac{4\sigma_{s/a} M_w}{RT \rho_w} \quad (2)$$

where S is the given supersaturation ratio (here 0.2 % used in this study), κ is the mean value of the hygroscopicity parameter calculated in Eq. (1).

2.2.2 Chemical components

For the inland atmospheric measurements, the non-refractory submicron aerosol (smaller than $1 \mu\text{m}$, NR-PM₁) chemical composition was quantitatively characterized using the Aerodyne High-Resolution Time-of-Flight Aerosol Mass Spectrometer (HR-ToF-AMS) (DeCarlo et al., 2006), including sulfate (SO_4^{2-}), nitrate (NO_3^-), ammonium (NH_4^+), chloride (Cl) and organics (Org). The black carbon (BC) mass concentration was determined from the light absorption with a seven-wavelength aethalometer (AE33, Magee Scientific Corp.).

Measurements of PM₁ in the coastal atmosphere were also performed by the HR-ToF-AMS, including major inorganic salts (non-sea-salt sulfate, nss- SO_4^{2-} ; methanesulfonic acid, MSA; NO_3^- ; NH_4^+) and organic matter. The sea salt was quantified using NaCl ion signal, which has been demonstrated in previous studies (Ovadnevaite et al., 2014). The instrument operation and calibration have been described in previous studies (Ovadnevaite et al., 2014; Xu et al., 2019).

2.2.3 Aerosol number size distribution and CCN number concentration

Particle number size distributions (PNSD) were measured using an integrated system consisting of a Differential Mobility Analyzer (DMA; model 3081, TSI Inc.) coupled with a Condensation Particle Counter (CPC; model 3772, TSI Inc.). During the measurements at IAP, the PNSD covered the size range of 10–550 nm with a 5 min time resolution. It scanned size range of 20–500 nm at MHD with a 10 min temporal resolution. The CCN number concentrations were quantified at both sites using a Droplet Measurement Technologies CCN counter (DMT-CCNc) (Lance et al., 2006). The instrument's supersaturation (SS) settings were carefully calibrated before and after each campaign using ammonium sulfate aerosol following Rose et al. (2008) (Fig. S1). Four effective supersaturations (SS) were 0.14 %, 0.23 %, 0.40 % and 0.76 % at IAP site. Four SS levels were 0.25 %, 0.5 %, 0.75 % and 1 % at MHD site with an uncertainty of ± 0.03 %. Using measurements at set supersaturation of 0.2 % as an example explores the CCN activity in the following discussions.

2.3 Calculation the heterogeneity for aerosol particles

To characterize the heterogeneous distribution of the hygroscopic and non-hygroscopic components in populations

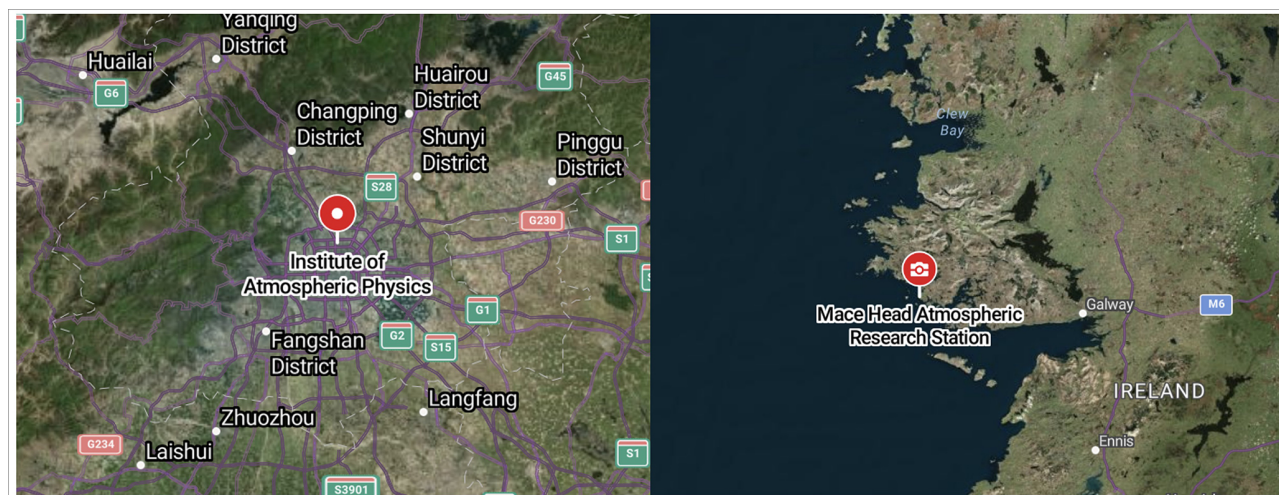


Figure 1. Map of the sites in the Inland of the Institute of Atmospheric Physics (IAP) and Coastal of Mace Head (MHD). (Imagery ©2025 Airbus, CNES/Airbus, Landsat/Copernicus, Maxar Technologies, NASA, Map data © 2025 Google, <https://maps.google.com/>, last access: 2 April 2025).

(Chen et al., 2022b), we calculated the mixing state index (χ) using the κ -PDF, following the methodology of Yuan and Zhao (2023). Two surrogate groups in a population of N aerosol particles were assumed (Zheng et al., 2021a). One surrogate group consists the non- and/or slightly hygroscopic species with κ_N of < 0.05 and another group contains the more hygroscopic species with κ_H of 0.5 – 0.6 (Yuan and Zhao, 2023, referred inorganics). Ambient particles typically contain one or two of the components and the κ lies between 0 and 0.6 at IAP or 0.8 at MHD as shown in Fig. S2. Taking into account the enhanced hydrophilicity of marine aerosols at MHD site, calculation assuming κ_H values of 0.7 and 0.8 were shown in Fig. S3. While these variations in κ_H introduced a mean uncertainty of 8% in χ values, it did not significantly affect the seasonal or site comparisons. The volume fraction of two surrogate groups can be calculated based on the total κ according to the Zdanovskii–Stokes–Robinson (ZSR) mixing rule (Zdanovskii, 1948; Stokes and Robinson, 1966).

The mixing state index χ is defined as the affine ratio of the average particle species diversity (D_α) and population species diversity (D_γ) as:

$$\chi = \frac{D_\alpha - 1}{D_\gamma - 1} \quad (3)$$

The average per-particle species diversity D_α can be calculated as follows. First, the mixing entropies at bin i (H_i) are determined according to Eq. (4),

$$H_i = -P_{i,N} \times \ln P_{i,N} - P_{i,H} \times \ln P_{i,H} \quad (4)$$

where $P_{i,N}$ and $P_{i,H}$ are the volume fraction of each group for the κ -PDF with X bins at bin i ($i = 1, 2, \dots, X$), and can be determined from the $P_{i,N} + P_{i,H} = 1$ and $P_{i,N} \times \kappa_N + P_{i,H} \times$

$\kappa_H = \kappa_i$. Here $\kappa_N = 0.01$, $\kappa_H = 0.6$; κ_i represents the hygroscopicity parameter at bin i .

Based on the assumption that particles in the same diameter have the same mixing entropy $H_\alpha = \sum_{j=1}^N P_j \times H_j$, $P_j = \frac{V_j}{V_{\text{total}}} = \frac{1}{N}$; the per-particle mixing entropies H_α is determined according to Eq. (5),

$$H_\alpha = \sum_{i=1}^X H_i \times c(\kappa)_i \times \Delta\kappa \quad (5)$$

where $c(\kappa)_i$ is the probability density of the normalized κ -PDF at bin i , and $\Delta\kappa$ represents the bin width. Then, the average per-particle species diversity D_α can be determined as $D_\alpha = e^{H_\alpha}$.

The bulk population species diversity D_γ can be calculated as follows. First, the aerosol population of the mixing entropy can be calculated as Eq. (6):

$$H_\gamma = -P_N \times \ln P_N - P_H \times \ln P_H \quad (6)$$

where P_N and P_H are the volume fraction of the non-hygroscopic and hygroscopic components in the population, and can be calculated by Eqs. (7) and (8):

$$P_N = \sum_{i=1}^X P_{i,N} \times c(\kappa)_i \times \Delta\kappa \quad (7)$$

$$P_H = \sum_{i=1}^X P_{i,H} \times c(\kappa)_i \times \Delta\kappa \quad (8)$$

Then, the bulk population species diversity D_γ can be determined as $D_\gamma = e^{H_\gamma}$. Here, the definition of surrogate species as supersets encompassing hygroscopicity heterogeneity implies that the heterogeneity parameter χ ranges from 0 to 1 . When the mixing index χ approaches 0 , it indicates a completely segregated state where hygroscopic and non-hygroscopic species reside in distinct particles. For

the case where the mixing index χ is 1, it represents a homogeneous distribution of non-hygroscopic and hygroscopic species throughout the aerosol population.

3 Result and discussion

3.1 Comparison of the heterogeneity in the inland and coastal atmosphere

To characterize the hygroscopic heterogeneity of atmospheric aerosols, Fig. 2 depicts variations in mixing state metrics ($D\alpha$, $D\gamma$, χ) and the hygroscopic parameter (κ_{Gf}) across particle size distributions. The $D\alpha$ and χ decrease with increasing particle diameter, accompanied by higher κ_{Gf} values at IAP site. This trend indicates that inland particle populations tend to homogenize into hygroscopic compositions through primary particle aging or secondary formation processes (Liu et al., 2025; Chen et al., 2022b; Zhong et al., 2022). In contrast, particles exhibit a non-monotonic pattern at MHD site: $D\alpha$ and χ decrease for Aitken-mode particles (< 100 nm) but increase for accumulation-mode particles. The κ_{Gf} shows consistent size-dependent increases in both winter and summer campaigns.

Notably, the mixing state metrics exhibit a pronounced minimum at 75 nm particles, influenced by distinct mechanisms: winter minima reflect the high sea salt fraction, while summer minima are driven by anthropogenic organic matter (Cheung et al., 2020; Xu et al., 2021a). Lower winter χ values – coupled with broader κ -PDF distributions – indicate stronger external mixing and compositional diversity compared to summer (Fig. S2). Seasonal χ and κ_{Gf} disparities are more pronounced at MHD site, primarily driven by the seasonal alternation of marine and anthropogenic emission sources.

Ultrafine particles (40 nm in IAP vs. 35 nm in MHD, Aitken mode) and larger particles (150 nm in IAP vs. 165 nm in MHD, accumulation mode) are selected to investigate distinct evolutionary processes of aerosol heterogeneity (Figs. 3 and S4). With the increasing of PM_{10} concentration during winter, the variation in χ values exhibit only minor both at the IAP and MHD sites, generally fluctuating between approximately -0.04 and 0.08 (Fig. 3a and c). Inland accumulation-mode particles show a modest increase in χ , corresponding with a higher proportion of inorganic salts. Conversely, at MHD site, the composition fraction shifts from a sea-salt dominance toward organic matter, accompanied by a $\sim 20\%$ increase in nitrate content (Fig. 3c). In summer, the variation of χ with PM concentration becomes markedly pronounced at both IAP and MHD stations. For example, χ for 40 nm particles decreases as PM increases at IAP site (Fig. 3b). The elevated particle heterogeneity mainly arises from the locally primary emissions, corresponding to the enhanced primary organic emissions as shown in Fig. S5. It appeared more pronounced during evening rush hours. In contrast, χ for 150 nm particles increases from ~ 0.40 to

~ 0.60 with rising PM, reflecting enhanced secondary formation and internal mixing during pollution process that render the particle population more homogeneous. At coastal sites, χ declines with rising PM by approximately 0.37 for 35 nm particles and 0.24 for 165 nm particles, mirroring the shift in chemical composition makeup from inorganic dominance to greater organic content (Fig. 3d).

Diurnal variations of mixing state metrics ($D\alpha$, $D\gamma$, Gf-PDF and χ) at IAP and MHD sites are shown in Fig. 4. In IAP-winter, particles exhibited steeper declines in $D\alpha$ and χ during evening rush hours than summer, indicating a higher fraction of non-hygroscopic particles (40 nm) from fresh traffic emissions (Figs. 4a1 and S5). Concurrently, reduced $D\gamma$ values suggest that the bulk population consists of uniformly distributed less-hygroscopic (LH) components (Fig. 4c1). Aitken mode particles showed bimodal and broader Gf-PDF distributions, corresponding to cooking activities (11:00–13:00 LT) and traffic peaks (17:00–20:00 LT) (Cai et al., 2020). Midday photochemical aging promoted more internally mixed aerosols (Yang et al., 2012; Liu et al., 2025), as evidenced by increasing $D\alpha$ at the urban site (Fig. 4b1). Conversely, the χ for accumulation-mode particles showed minimal diurnal variations both in IAP-winter and IAP-summer. This is mainly due to the dominant hygroscopic mode for 150 nm particles (Fig. 4g1 and h1), especially during summer, which is mainly from secondary formation or aging of the primary particles (such as the transformation from primary organic aerosol (POA) to secondary organic aerosol (SOA) in Fig. S5) (Wang et al., 2019; Fan et al., 2020).

For the coastal atmosphere, the mixing state metrics ($D\alpha$, $D\gamma$, and χ) of Aitken and accumulation mode particles in winter exhibited analogous diurnal patterns, characterized by a descending trend at nightfall (Fig. 4a2–h2). This corresponds to an enhanced modal distribution of near-hydrophobic (NH) particles at 35 nm and more-hygroscopic (MH) particles at 165 nm. In summer, $D\alpha$ and $D\gamma$ both trended downward during daytime, with the decline of $D\gamma$ being more pronounced. A conspicuous seasonal discrepancy between Aitken and accumulation mode particles was observed in this region (Fig. 4a2–h2), where the mixing state index χ increased incrementally from winter to summer. Specifically, the mean χ for 35 nm particles escalated from 0.42 to 0.80, and for 165 nm particles, it rose from 0.39 to 0.76. This trend demonstrates a strong alignment with the spread factor (used as a measure of particle mixing state) documented by Xu et al. (2021a).

Similar to the mixing state χ , a very clear seasonal pattern of the aerosol hygroscopic distribution was found (Fig. 4e–h). In winter, the Gf-PDF diurnal profiles of both Aitken and accumulation mode particles showed bimodal distribution (Fig. 4e2–g2) as evident by the number fraction of nearly-hydrophobic and more hygroscopic modes (Fig. S6). The NH mode is likely composed of anthropogenic organic matter and biogenic species derived from marine air masses (Xu

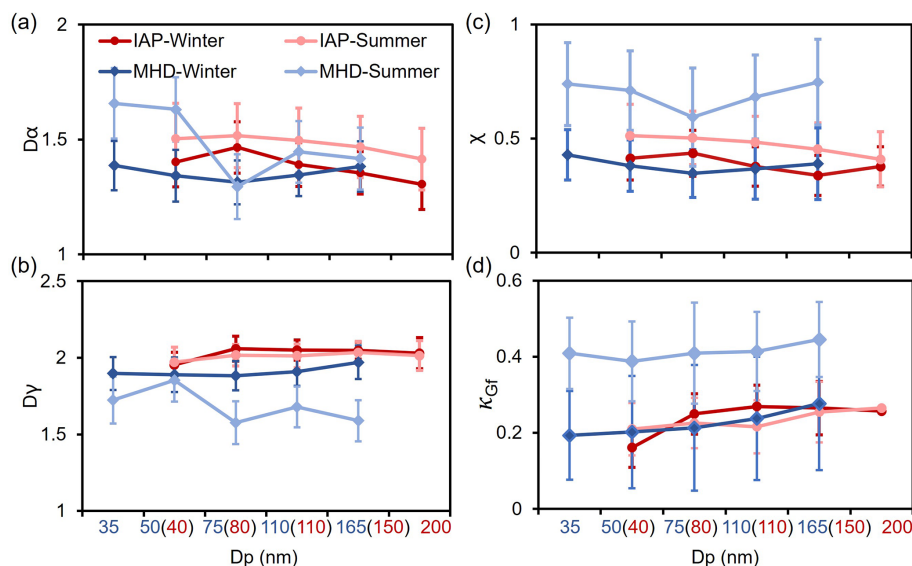


Figure 2. Mean values of the $D\alpha$ (a), $D\gamma$ (b), χ (c) and κ_{Gf} (d) for aerosols of five diameters during winter and summer periods at IAP and MHD sites.

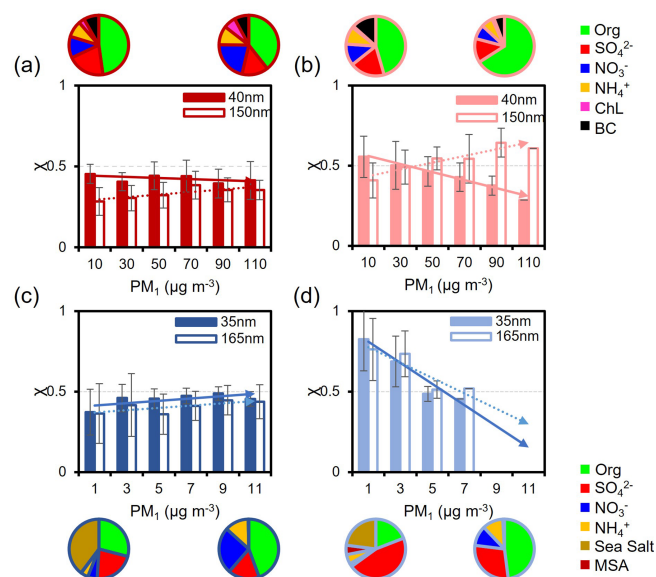


Figure 3. Variation of the average χ for 40 and 150 nm particles at IAP and 35 nm and 165 nm at MHD site with the particle mass concentration in IAP-winter (a), IAP-summer (b), MHD-winter (c) and MHD-summer (d). The pie charts represent the average mass fraction during four field measurements.

et al., 2020), with this composition being particularly prominent in the Aitken mode. Additionally, Xu et al. (2021a) observed a higher abundance of the NH-mode in marine polar and Arctic air masses, this further supports the notion that NH particles are likely of biogenic origin, aside from contributions from anthropogenic activities. The more hygroscopic and sea salt mode was mostly contributed from the

nss-sulfate and sea salt in winter (Xu et al., 2021a). Analogously, accumulation mode particles with a higher proportion of MH and SS mode (Fig. S6) primarily attributed to the prevalence of non-sea-salt sulfate (nss-sulfate) and sea salt in the coastal atmosphere (Xu et al., 2020). The bimodal and broad of hygroscopic distribution suggested that particles were more diverse and external mixed, consistent with the lower χ value in winter.

In contrast, summer observations revealed that Gf-PDFs of both Aitken and accumulation mode particles transitioned to unimodal distributions, signifying particles in summer had more homogeneous composition with a large extent of internal mixing particles (with higher χ). Such diurnal trend in Gf-PDFs was consistent along with the high number fraction of MH-mode and low NH-mode (Fig. S6). The higher hygroscopicity and MH mode in summer were largely driven by the enhancement of sulfate and decrease of organic matter (Fig. S6). And a clear shift from NH to MH mode at midday might further demonstrate the promotion of photochemical aging in summer (Xu et al., 2021a).

3.2 Impacts of primary aerosol emissions and secondary aerosol formation on aerosol mixing state

As already noted above, changes in χ were clearly associated with the chemical composition varying with site and season. The relationships between the mixing state index and the number fraction of hydrophobic and hygroscopic mode during four campaigns are presented in Fig. S7. The χ exhibited negative correlations with the fraction of hydrophobic mode but a positive relationship with the fraction of hygroscopic particles, highlighting the markedly different effects of the primary emissions and secondary formation on aerosol mix-

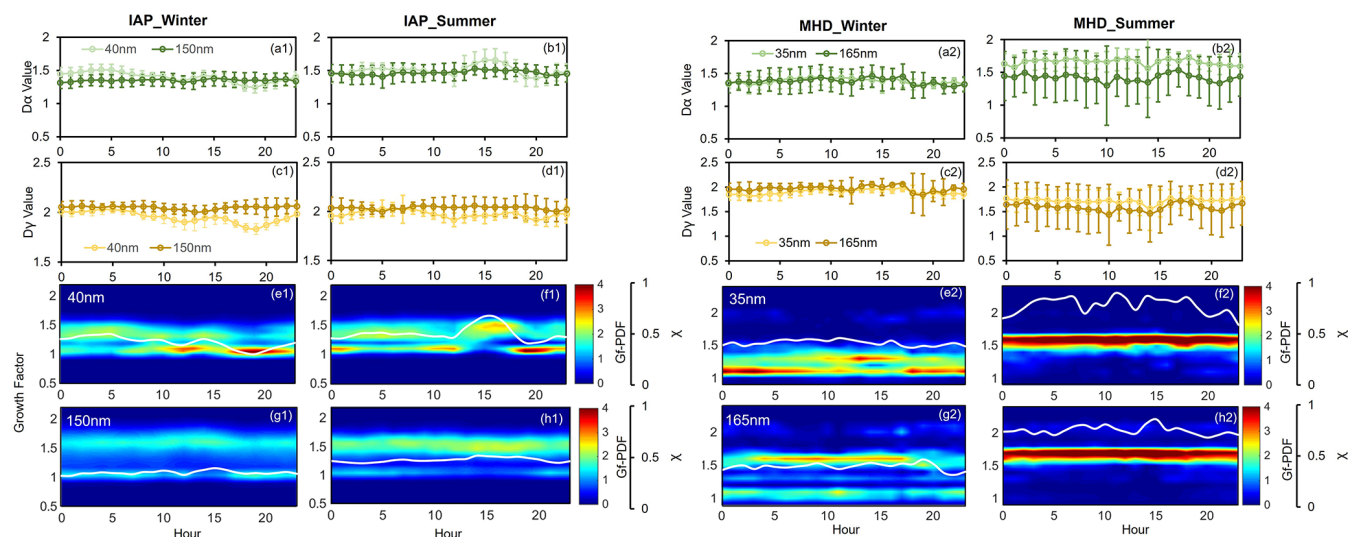


Figure 4. Diurnal variation of $D\alpha$, $D\gamma$, Gf-PDF, and χ during winter and summer periods for 40 and 150 nm aerosols at IAP (a1–h1) and for 35 and 165 nm aerosols MHD site (a2–h2).

ing state (Tao et al., 2024). To gain more insight on this effect between inland and coastal atmosphere, four cases are analyzed (Figs. 5 and 6): case for IAP-winter, case for IAP-summer, case for MHD-winter and case for MHD-summer.

Case for IAP-winter is a heavy polluted event with the mean PM mass concentration increased from 22 to $437 \mu\text{g m}^{-3}$ (Fig. 5a–d). The 40 and 150 nm χ patterns shifted quickly during the pollution periods. With the mass fraction of hydrophobic compounds (i.e., POA) in PM₁ increased, the χ of 40 nm particles decreased from 0.5 to 0.2, that is, an enhanced NH mode and a weakened MH mode (Fig. 5b–c). At this stage, large particles for 150 nm are mainly from aqueous formation with more proportion of nitrate. The corresponding χ of 150 nm particle was higher. While with that the mass fractions of secondary organic and inorganic compositions increased, particles were more internally mixed with χ increased to be 0.6 for 40 nm and 0.53 for 150 nm particles.

Case for IAP-summer is the typical new particle formation events (NPF) with the mean PM₁ of $13 \mu\text{g m}^{-3}$ (Fig. 5a1–d1). With the evolution of NPF events, the χ of 40 and 150 nm particles increased to be 0.95 and 0.61 with the enhanced proportion of more-hygroscopic components (i.e., SOA, NO_3^- , SO_4^{2-}). The χ pattern is opposite of that the number fraction of NH mode and consistent with the variation of MH mode (Fig. S7). Note that a sudden decrease in χ on 11 June was disturbed by the strong primary emission. The chemical mass fractions showed more POA and black carbon with an enhanced NH mode and a weaker MH mode (Fig. 5b1–d1). The χ of 40 nm particles decreased to be 0.4 and that of the 150 nm particles decreased to be 0.2. The χ patterns appear to similar transitions for Aitken and accumulation-mode particles during haze and NPF events. The increase in

χ is synchronous with the increase in MH mode from secondary formation but opposite with that of LH mode from primary emissions. This implies that the primary emissions would lead particles more external mixing while secondary formation would promote aerosol more internal mixed in Inland atmosphere.

Case for MHD-winter is a high organic matter pollution event with the mean PM₁ of $5.2 \mu\text{g m}^{-3}$ and 52 % mass fraction of organics (Fig. 6a–d). Larger presence of anthropogenic organic matter resulted the NH mode for 35 nm particles to be 95 % and 165 nm particles to be 53 % (Fig. 6). The χ of 35 and 165 nm particles decreased with the NH mode increased (Fig. S7), similar with the case for IAP site. There was a steady increase in χ when the MH-mode particles started increasing with the increase in mass fraction of inorganics, e.g., 35 nm particles showed the mean χ increasing from 0.43 to 0.57 and 165 nm particles from 0.35 to 0.6. This indicated that the trend of aerosol mixing state closely followed the evolution of emission and secondary formation.

Case for MHD-summer is an extremely clean event with the mean PM₁ of $0.7 \mu\text{g m}^{-3}$ (Fig. 6a1–d1). The dominated MH mode was found throughout the case, which could be attributed from the high mass fraction of nss-sulfate (41 % average). Compared with the case in MHD-winter, the mean proportion of organic has decreased to be 15 %. Therefore, the χ remains at a high value (mean χ of 0.9 for 35 nm and 0.8 for 165 nm particles). Until 28 August, a stronger increase in the mass fraction of sea salt and accordingly SS mode in larger-size particles was observed. The χ decreased rapidly with the decrease in MH mode and enhanced SS mode, especially for the accumulation mode particles, suggesting the sea spray production makes particles more externally mixed.

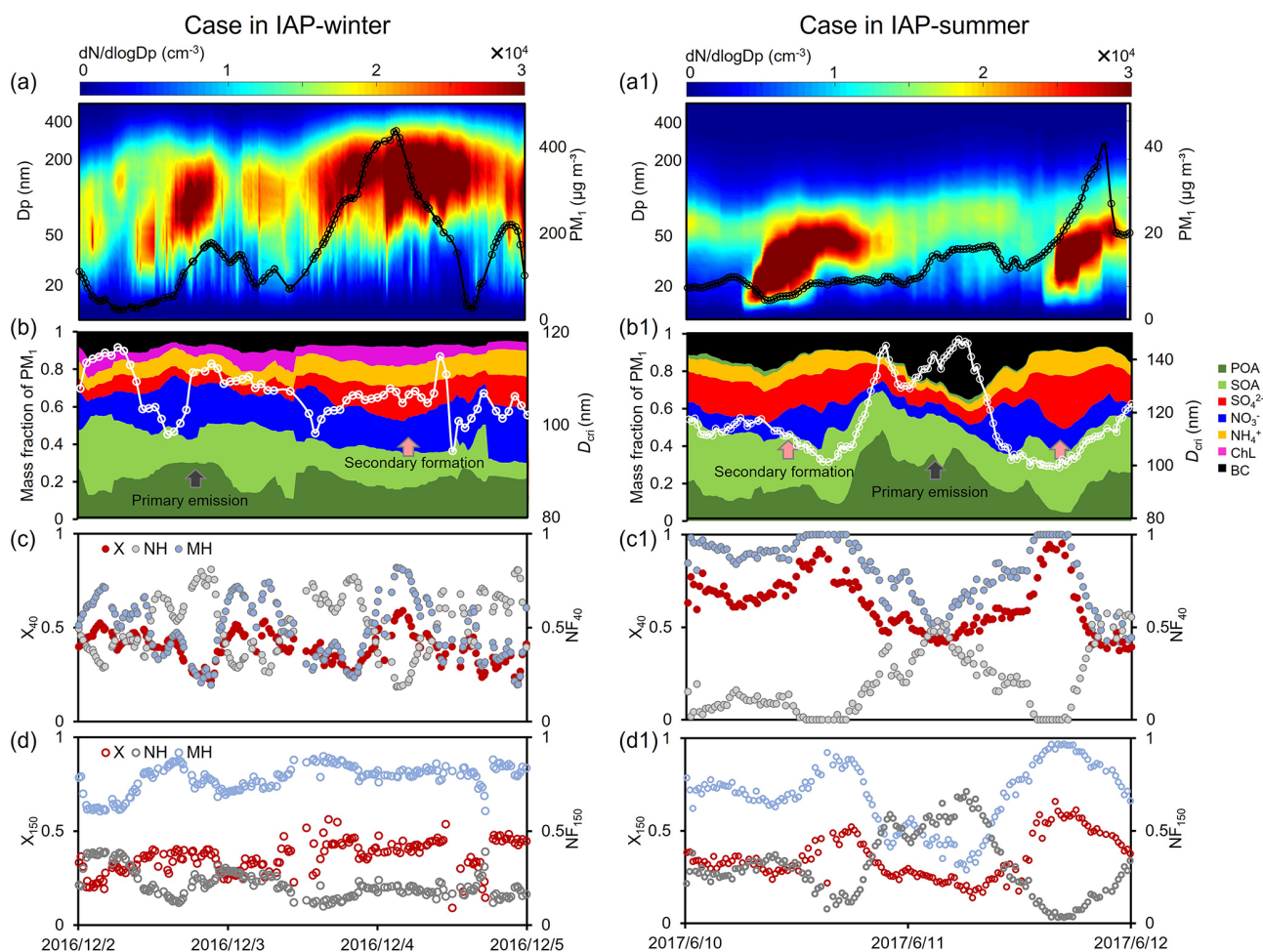


Figure 5. Case in IAP-winter (a–d) and IAP-summer (a1–d1). Particle number size distribution and PM_{10} (a, a1), mass fraction of the PM_{10} and the critical diameter (D_{crit}) (b, b1), mixing state index (χ), number fraction of the nearly hydrophobic mode (NH) and more hygroscopic mode (MH) for 40 nm particles (c, c1), χ , NH and MH for 150 nm particles (d, d1).

In summary, these results suggest that the primary emission and secondary formation drive the hygroscopic distribution and can result in significant variation of aerosol mixing state χ both in inland and coastal atmosphere. The pattern of χ varied among site and season, highlighting the importance of considering the impact of mixing state on CCN activity.

3.3 Covariation relationships between the mixing state and ccn activity

The mixing state of particle populations undergoes dynamic transformations during atmospheric aging, profoundly influencing their CCN activity. Unlike prior CCN closure studies that assumed mixing states based on chemical component fractions (Yang et al., 2012; Padró et al., 2012; Ren et al., 2018), this work employs the hygroscopicity distribution- and entropy-derived mixing state index χ to clarify the covariation relationships between the mixing state and CCN activity. Given that CCN activity reflects the characteristics of

the entire particle population while χ is calculated from HT-DMA measurements at specific particle diameters, this study chooses the N_{CCN} , activation ratio (AR) at supersaturation of 0.2 % and the mean χ for accumulation-mode to illustrate the covariation characteristic approximately. This approach is employed to ensure that both variables/parameters reflect the characteristics of the accumulation-mode particle population. The covariations of particle size and chemical composition with the mixing state (χ ranging from 0 to 1 at intervals of 0.1) are illustrated in Fig. 7. This figure provides key insights into two fundamental determinants of CCN activity (Dusek et al., 2006).

As χ increases, the peak diameter (D_{peak}) of the particle number size distribution (PNSD) shifts toward larger sizes (Figs. 7a and S8), while peak concentrations occur within the intermediate χ range (0.3–0.6). This trend indicates that CN number concentration (N_{CN}) first increases, driven by primary emissions and new particle formation, then decreases due to mixing and aging processes (Fig. 7b). No-

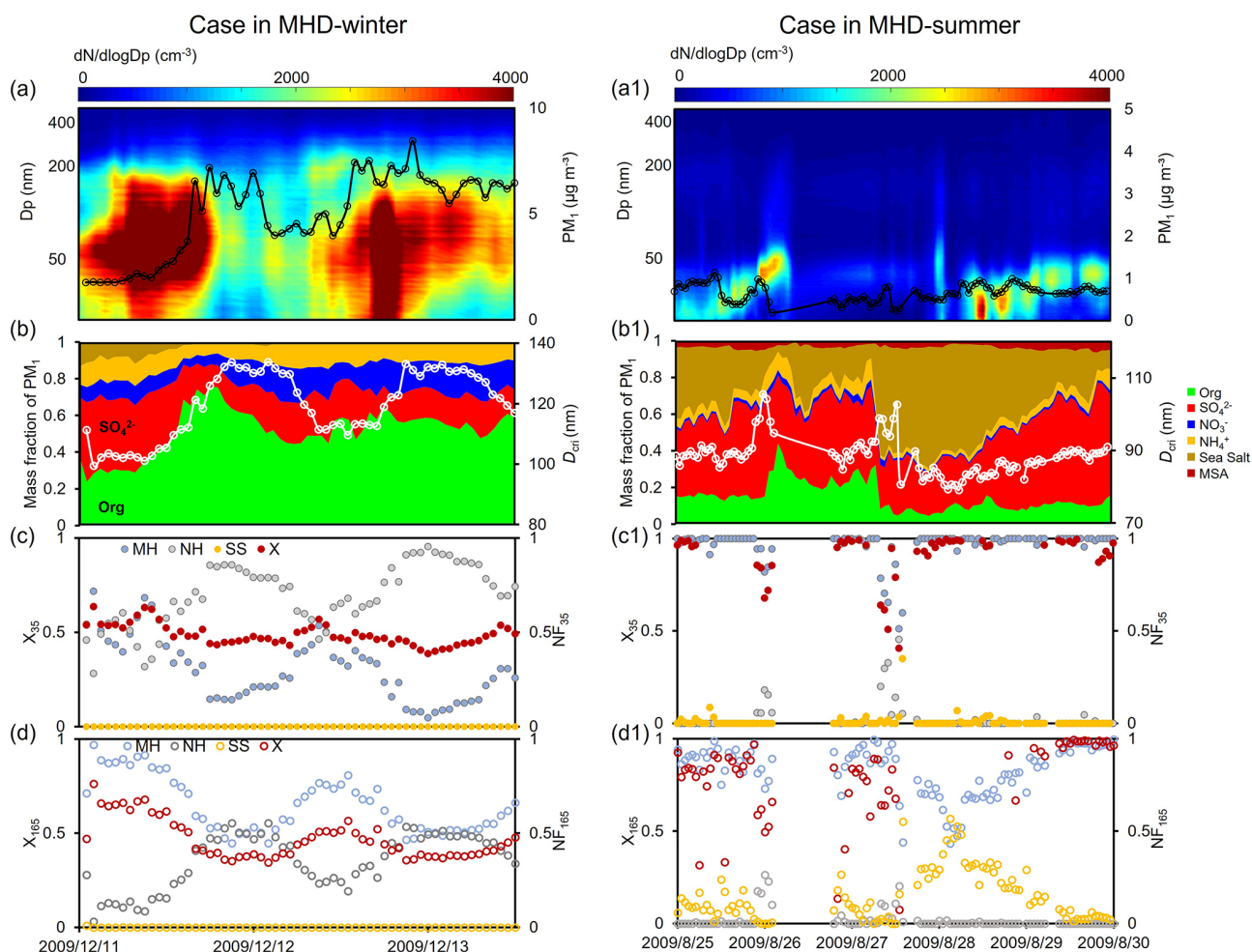


Figure 6. Case in MHD-winter (a–d) and MHD-summer (a1–d1). Particle number size distribution and PM_{10} (a, a1), mass fraction of the PM_{10} and the critical diameter (D_{crit}) (b, b1), mixing state index (χ), number fraction of the nearly hydrophobic mode (NH) and more hygroscopic mode (MH) for 35 nm particles (c, c1), χ , NH and MH for 165 nm particles (d, d1).

tably, new particle formation events frequently occurred in IAP-summer (Fig. S9), corresponding the gradually increase of χ . And the χ for Aitken-mode is significantly larger than the accumulation-mode particles during this period. Thus, N_{CN} exhibits a sustained slight increase as the degree of the internal mixing increases in IAP-summer.

The critical diameter (D_{crit}) – defined as the minimum size required for activation at a given supersaturation – depends on aerosol hygroscopicity. In turn, this hygroscopicity is jointly determined by the hygroscopicity of individual soluble components and their mass fractions in the aerosol (Petters and Kreidenweis, 2007). Using measurements at supersaturation of 0.2% as an example, Fig. 7c shows that D_{crit} decreases with increasing highly hygroscopic inorganic components (e.g., sulfate, nitrate) in the inland atmosphere. In contrast, coastal D_{crit} exhibits nonlinear variations with χ : high external mixing (low χ) elevates D_{crit} due to dominant organic components, reducing sea salt particle fractions. As

χ increases, the mass fraction of non-sea-salt sulfate (nss-sulfate) rises, enhancing activation potential by decreasing D_{crit} .

The covariation characteristic of CCN activity at 0.2% supersaturation with mixing state index χ reveals distinct inter-atmospheric differences, as shown in Fig. 7d–e. In IAP, N_{CCN} at $S = 0.2\%$ demonstrates a monotonic increasing trend with χ , attributed to the synergistic effects of rising N_{CN} and decreasing D_{crit} (Fig. S10). By contrast, coastal N_{CCN} follows a pattern analogous to N_{CN} , with peak concentrations shifting toward higher χ values. This highlights the dominant role of particle size effects in enhancing CCN concentrations under marine-influenced conditions (Dusek et al., 2006).

Two distinct D_{crit} - χ trends underpin these disparities: one remains stable, driven by the inherent hygroscopicity of sea salt, while the other exhibits steep D_{crit} declines associated with anthropogenic pollution as internal mixing intensifies.

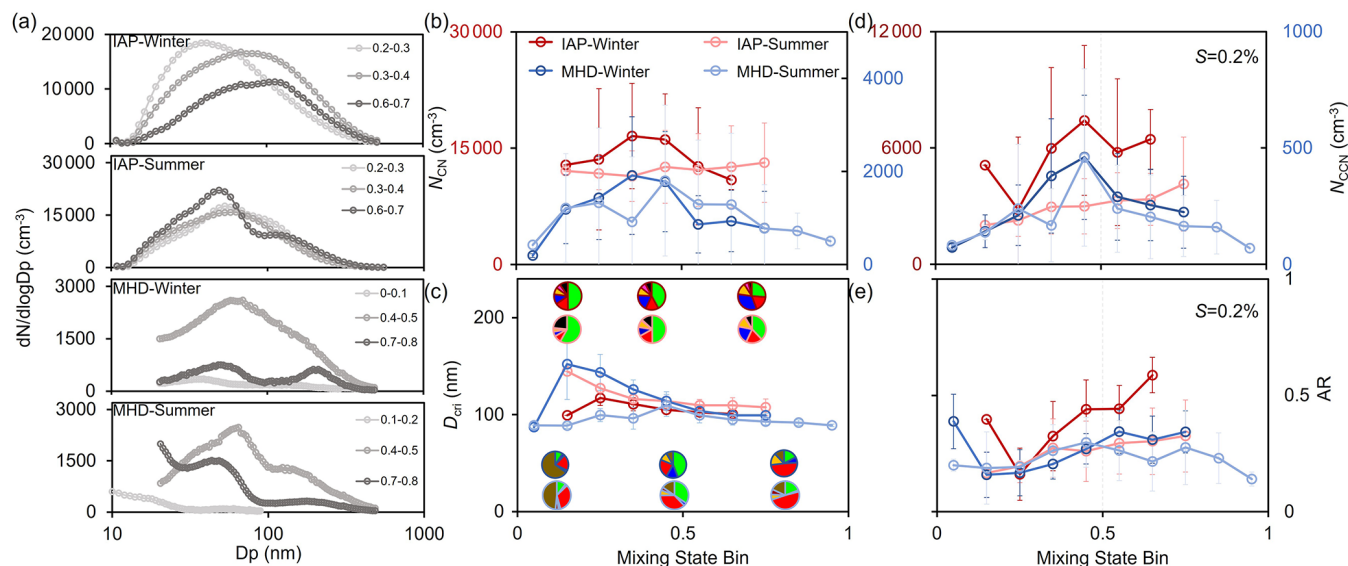


Figure 7. Comparison of the average particle number size distribution (PNSD) in different mixing state index (χ) (a), CN number concentration (N_{CN}) as a function of χ (b), Critical diameter (D_{crit}) at $S = 0.2\%$ and mass fraction of chemical composition as a function of χ (c), CCN number concentration (N_{CCN}) (d) and activation ratio (AR) at $S = 0.2\%$ a function of χ (e).

These discrepancies are further manifested in the nonlinear D_{crit} - χ relationship. The activation ratio (AR) – quantifying aerosol cloud droplet formation potential at fixed supersaturation – also varies by site (Fig. 7e). Notably, AR shows a marked increase with χ in IAP-winter, likely due to enhanced N_{CCN} from the elevated inorganic fraction under higher mixing states (Fig. 3). Conversely, the inorganic fraction decreases during other sampling periods, dampening AR growth.

The mixing state directly reflects the degree of particle aging, which subsequently influences the particle composition and size. Figure 8 further examines the covariation characteristics of CN concentration, chemical compositions (i.e., D_{crit}) with mixing state across particle populations. The mixing state index quantifies the variance in hygroscopic distribution that emerges directly from compositional heterogeneity. Thus, it can indirectly affect D_{crit} by serving as an indicator of particle aging. The critical diameter (D_{crit}) is intrinsically sensitive to the hygroscopic distribution – wherein broader hygroscopic spectra (corresponding to lower χ) engender more extensive D_{crit} ranges. As shown in Fig. 8a, the D_{crit} exhibits heightened sensitivity to minor χ fluctuations in the mixing state (χ) when $\chi < 0.5$. This significant decrease in D_{crit} with increasing χ further confirms the potential effect of aging degree on critical particle diameter. In contrast, for particles already characterized by internal mixing, further increases in χ (i.e., higher degrees of internal mixing) exert a negligible influence on D_{crit} . Particularly when $\chi > 0.7$, the variation in D_{crit} with χ is within 20%. This behavior pattern reflects the influence of hygroscopic heterogeneity on critical diameter and might enable a novel parameterization for

D_{crit} estimation. This behavior pattern implies that the D_{crit} - χ relationship could enable a novel parameterization for D_{crit} estimation when the aerosol particles are not highly aged or when the internal mixing degree of aerosol particles is relatively low, serving as a novel framework for integrating mixing state effects on CCN activity in atmospheric models.

Aerosol observation at MHD site (blue dots) span a broad D_{crit} range (80–220 nm) with χ varying from 0.1 to 1, reflecting alternating influences of highly hygroscopic inorganic salts (sea salt, sulfate) and less-hygroscopic organic matter. In contrast, observation at IAP site that is dominated by anthropogenic aerosols exhibit a narrower D_{crit} range (90–150 nm). Both environments show negative D_{crit} - χ correlations, but with distinct functional forms. For instance, MHD aerosols feature an exceptional logarithmic fit ($D_{crit} = -42.98 \ln(\chi) + 80.36$, Pearson $r = -0.87$, $R^2 = 0.75$; Fig. 8a blue line), while IAP aerosols (red line) yield a shallower slope (-12.04) and Pearson r of -0.4 . This quantifies that D_{crit} sensitivity to χ is 3.6 times steeper in MHD environments. This behavior pattern implies that the D_{crit} - χ relationship could enable a novel framework for D_{crit} estimation. The slope reflects the compositional diversity of the regime, steeper slopes occur where small χ variations correspond to large compositional shifts (e.g., sea salt in coastal site). As discussed above, strong impact of primary emission and secondary formation on aerosol mixing state was observed in both sites (Figs. 5 and 6). One could obtain more details on the D_{crit} - χ correlations. For example, the D_{crit} exhibited rapidly increase with the increase of primary emissions (i.e., mass fraction of POA enhanced) during polluted periods. The D_{crit} pattern appeared opposite with that

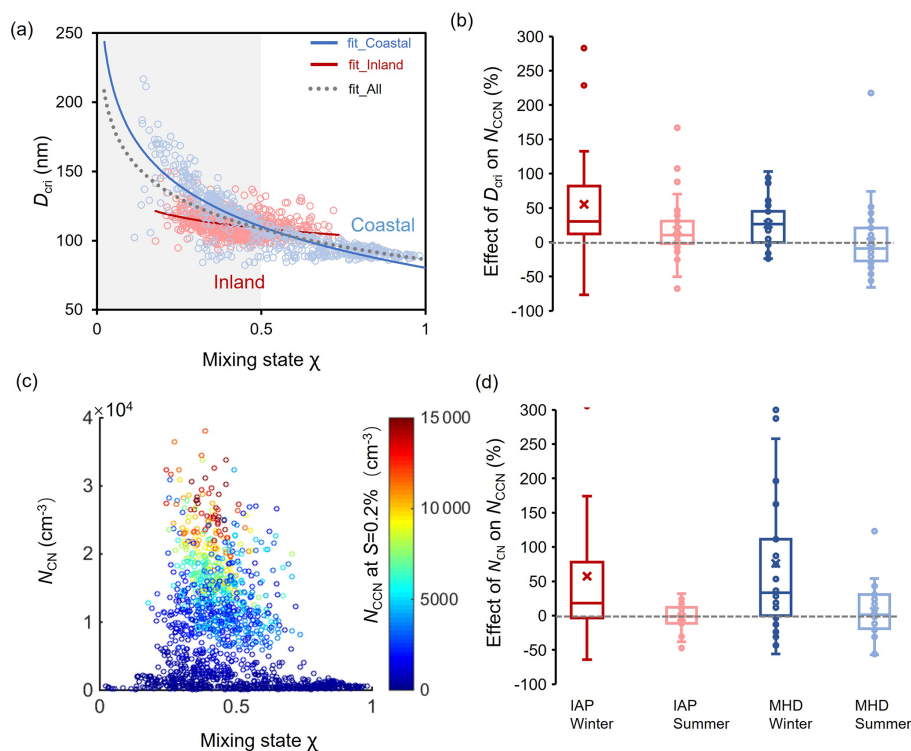


Figure 8. Covariation characteristics of the critical diameter (D_{cri}) with the χ (a), relative change of CCN number concentration (N_{CCN}) at supersaturation $S = 0.2\%$ with the reduction in D_{cri} (b); Covariation characteristics of the CN number concentration (N_{CN}) with the χ , different colors represent the N_{CCN} (c), relative change of N_{CCN} with the change in N_{CN} (d).

of the mixing state index, especially for the accumulation-mode particles. More pronounced $D_{\text{cri}}-\chi$ correlations were observed during the new particle formation (Fig. 5a1–d1). The decreasing presence of D_{cri} matched the increasing proportion of SO_4^{2-} and SOA with the χ increased during NPF events. Similar correlations between the critical diameter and mixing state index were also found in the coastal atmosphere, especially for the case of the enhanced anthropogenic organic matter and sea salt production (Fig. 6). This implies that the relationship between the D_{cri} and χ might be disturbed by the variation of emission pollution and secondary formation processes, resulting in spatiotemporal differences. The D_{cri} reduces by 2.2%–6.8% with the mixing state increase at a step of 0.1, with the steepest winter decline (Fig. S11).

Changes in N_{CN} with differ starkly between environments: positive effects in polluted inland air (+9%) versus negative effects in coastal regions (−2%). Aerosols in IAP, frequently perturbed by primary emissions and new particle formation, exhibit elevated N_{CN} (peaking at $\chi = 0.2\text{--}0.7$), while in MHD N_{CN} remains $\sim 5000\text{ cm}^3$ across all χ . We categorized data into two groups: C1 (particles within specific N_{CN} ranges) evaluates N_{CCN} covariations mainly driven by $D_{\text{cri}}-\chi$ relationships, while C2 (particles within fixed D_{cri} intervals) assesses $N_{\text{CN}}-\chi$ effects (Fig. 8b). Relative changes (RC) in D_{cri} , N_{CN} , and N_{CCN} with χ were calculated by

comparing successive χ increments (χ_{i+1} vs. χ_i , $i = 0, 0.1 \dots 1$) within defined N_{CN} or D_{cri} windows.

Notably, the covariation relationship between the N_{CCN} and mixing state exerts more pronounced for the case of externally mixed aerosols dominated. For example, MHD-winter aerosols (high external mixing; $\chi_{\text{mean}} = 0.38 \pm 0.12$) showed RCs in N_{CCN} of 23% (C1) and 72% (C2), whereas MHD-summer aerosols (high internal mixing; $\chi_{\text{mean}} = 0.69 \pm 0.19$) exhibited negligible effects (−2.5% in C1, 0.9% in C2). Inland atmospheres, despite smaller seasonal χ variations, showed analogous trends: RCs of N_{CCN} in winter (55% in C1, 57% in C2 for external mixing) exceeded summer values for more internally mixed populations (Fig. 8d). These results confirm that hygroscopic heterogeneity strongly influences N_{CCN} under external mixing, aligning with prior work (Ching et al., 2017).

The covariation characteristics are most pronounced during winter in both environments, attributed to heightened winter D_{cri} sensitivity to χ : a 0.1 χ increase reduces D_{cri} by 5.2% (winter), boosting N_{CCN} by 39%, versus 2.4% D_{cri} reduction (summer) yielding only 6% N_{CCN} enhancement. Concomitantly, winter $N_{\text{CN}}-\chi$ effects on N_{CCN} reach 65%, far exceeding summer responses.

In contrast to previous evaluation methods that oversimplify mixing states (Ren et al., 2018; Xu et al., 2021b), the entropy-based framework employed in this study explicitly

characterizes the covariation between the CCN activity and transitions in the mixing state. Aerosols in IAP-winter are presumably shaped by intense urban pollution sources – including traffic emissions, residential heating, and cooking activities – thereby enriching the externally mixed particle fraction (Fan et al., 2020; Xie et al., 2020). Analogously, aerosols in MHD-winter exhibit dominant external mixing, consisting of near-hydrophobic and hydrophilic particle mixtures (Xu et al., 2021a). As illustrated in Fig. S2, the winter aerosol population exhibits bimodal or multimodal κ -PDF distributions – this pattern indicates a high degree of external mixing, with the aerosols characterized by chemically diverse compositions. Collectively, these results underscore the pivotal role of mixing state heterogeneity in modulating CCN activity across different environments.

4 Conclusions

The mixing state of aerosol populations undergoes complex transformations during atmospheric aging, altering the distribution of hygroscopic and non-hygroscopic components and thus influencing CCN activity (Xu et al., 2021a; Ching et al., 2017). This study derived a mixing state index (χ) from field-measured hygroscopicity distributions, systematically investigating the covariation relationship between the mixing state and CCN activity at two inland and coastal environments. Results provide field evidence that aerosol mixing states generally reside between purely internal and external extremes (Chen et al., 2022b). Aerosol mixing state is largely influenced by the primary emissions and secondary formation process. Externally-mixed particles with more hydrophobic-mode originate chiefly from primary emissions in IAP, while those of more sea-salt mode from sea spray in MHD. While it becomes more internally-mixed as the enhanced fraction of more-hygroscopic mode and decreased fraction of hydrophobic mode during the aging process. This highlights a dual regulatory mechanism of mixing state and its potential impact on hygroscopic distribution and CCN activity.

As χ increases, CN number concentrations (N_{CN}) first rise – driven by primary emissions and new particle formation—then decline due to condensation and coagulation during aging. The critical diameter (D_{cri}) exhibits heightened sensitivity to minor χ fluctuations when $\chi < 0.5$. In contrast, for particles already characterized by internal mixing, further increases in χ (i.e., higher degrees of internal mixing) exert a negligible influence on D_{cri} . Additionally, both environments show negative $D_{\text{cri}}-\chi$ correlations, but with distinct functional forms. We propose a practical approach for estimating D_{cri} from χ , applicable when the aerosol particles are not highly aged or when the internal mixing degree of aerosol particles is relatively low, serving as a novel framework for integrating mixing state effects on CCN activity in atmospheric models.

Entropy-based analyses further support the covariation relationships between the mixing state and N_{CCN} , especially for externally mixed aerosols. Current models often oversimplify aerosol mixing states as purely internal or external (Stevens and Dastoor, 2019; Bauer et al., 2013), the latter being particularly sensitive to organic matter (Ren et al., 2018; Bhattu and Tripathi, 2015). Such simplifications introduce significant biases in N_{CCN} estimation (Riemer et al., 2019; Ching et al., 2019). The $\chi-D_{\text{cri}}$ parameterization proposed here offers a novel approach to reduce model complexity in representing aerosol hygroscopicity and CCN activation, enabling more accurate simulations of aerosol CCN capacity. It is expected mitigate the underestimation in CCN compared with the complete external mixing assumption, while effectively alleviates the overestimation that arises from applying the complete internal mixing assumption in regions characterized by high external mixing (Zheng et al., 2021a). This advancement improves our understanding of aerosol-cloud interactions (IPCC, 2021; Rosenfeld et al., 2019), critical for refining climate effect assessments.

Data availability. All data used in the study are available at <https://doi.org/10.3974/geodb.2019.06.11.V1> (Fan et al., 2020) and <https://doi.org/10.17632/3dx6pnx869.1> (Xu et al., 2021a).

Supplement. Additional analysis results that were applied in this study. Example of calibration results of HTDMA and CCN used in this study (Fig. S1), mean values of the κ -PDF for aerosols of five diameters (Fig. S2), sensitivity of the hygroscopic parameter for the group of the hygroscopic species on the mixing state index χ (Fig. S3), time series of the average per-particle species diversity $D\alpha$, the bulk population species diversity $D\gamma$, and their affine ratio χ (Fig. S4), diurnal trend of particle size, chemical mass fraction and number fraction (NF) of hydrophobic and hygroscopic mode in IAP (Fig. S5) and in MHD (Fig. S6), mixing state as a function of number fraction of hydrophobic and hygroscopic mode (Fig. S7), variation of the peak diameter (D_{peak}) with the mixing state index (Fig. S8), particle number size distribution and mixing state during new particle formation events (Fig. S9), diurnal variation of χ and CN concentration during winter and summer periods for 40 and 150 nm aerosols in inland and for 35 and 165 nm aerosols in coastal site (Fig. S10), relative change of the critical diameter and CN concentration with the mixing state index χ (Fig. S11) (PDF). The supplement related to this article is available online at <https://doi.org/10.5194/acp-26-2985-2026-supplement>.

Author contributions. RJH and JR conceived the conceptual development of the paper. JR, FZ and WX directed and performed the experiments with YW and LC. FZ and YS provided the dataset in the inland site. JO, DC and CO provided the dataset in the coastal site. JR conducted the data analysis and wrote the draft. All authors edited and commented on the various sections of the paper.

Competing interests. The contact author has declared that none of the authors has any competing interests.

Disclaimer. Publisher's note: Copernicus Publications remains neutral with regard to jurisdictional claims made in the text, published maps, institutional affiliations, or any other geographical representation in this paper. The authors bear the ultimate responsibility for providing appropriate place names. Views expressed in the text are those of the authors and do not necessarily reflect the views of the publisher.

Acknowledgements. This work was funded by the National Natural Science Foundation of China (NSFC) under grant nos. 42525301, 42405118 and 42475112, the State Key Laboratory of Loess Science, Institute of Earth Environment, Chinese Academy of Sciences (SKLLQG2429), the Guangdong Natural Science Foundation (grant no. 2024A1515011005), Shenzhen Science and Technology Program (grant nos. KCXST20221021111404011, SYSPG20241211173609007). We thank all participants of the field campaign for their hard work and sharing of the data.

Financial support. This research has been supported by the National Natural Science Foundation of China (NSFC) under grant nos. 42525301, 42405118 and 42475112, the State Key Laboratory of Loess Science, Institute of Earth Environment, Chinese Academy of Sciences (SKLLQG2429), the Guangdong Natural Science Foundation (grant no. 2024A1515011005), Shenzhen Science and Technology Program (grant nos. KCXST20221021111404011, SYSPG20241211173609007).

Review statement. This paper was edited by Mingjin Tang and reviewed by three anonymous referees.

References

- Bhattu, D. and Tripathi, S. N.: CCN closure study: Effects of aerosol chemical composition and mixing state, *Journal of Geophysical Research: Atmospheres*, 120, 766–783, <https://doi.org/10.1002/2014JD021978>, 2015.
- Bellouin, N., Quaas, J., Gryspeerdt, E., Kinne, S., Stier, P., Watson-Parris, D., Boucher, O., Carslaw, K. S., Christensen, M., Daniau, A.-L., Dufresne, J.-L., Feingold, G., Fiedler, S., Foster, P., Gattelman, A., Haywood, J. M., Lohmann, U., Malavelle, F., Mauritsen, T., McCoy, D. T., Schulz, M., Schwartz, S. E., Sourdeval, O., Storelvmo, T., Toll, V., Winker, D., and Stevens, B.: Bounding global aerosol radiative forcing of climate change, *Rev. Geophys.*, 58, e2019RG000660, <https://doi.org/10.1029/2019RG000660>, 2020.
- Bauer, S. E., Ault, A., and Prather, K. A.: Evaluation of aerosol mixing state classes in the GISS modelE-MATRIX climate model using single-particle mass spectrometry measurements, *Journal of Geophysical Research: Atmospheres*, 118, 9834–9844, <https://doi.org/10.1002/jgrd.50700>, 2013.
- Charlson, R. J., Schwartz, S. E., Hales, J. M., Cess, R. D., Coakley Jr., J. A., Hansen, J. E., and Hofmann, D. J.: Climate forcing by anthropogenic aerosols, *Science*, 255, 423–430, <https://doi.org/10.1126/science.255.5043.423>, 1992.
- Chen, Y., Haywood, J., Wang, Y., Malavelle, F., Jordan, G., Partridge, D., Fieldsend, J., Leeuw, J. D., Schmidt, A., Cho, N., Oreopoulos, L., Platnick, S., Grosvenor, D., Field, P., and Lohmann, U.: Machine learning reveals climate forcing from aerosols is dominated by increased cloud cover, *Nature Geoscience*, 15, 609–614, <https://doi.org/10.1038/s41561-022-01027-9>, 2022a.
- Chen, L., Zhang, F., Zhang, D., Wang, X., Song, W., Liu, J., Ren, J., Jiang, S., Li, X., and Li, Z.: Measurement report: Hygroscopic growth of ambient fine particles measured at five sites in China, *Atmos. Chem. Phys.*, 22, 6773–6786, <https://doi.org/10.5194/acp-22-6773-2022>, 2022b.
- Ching, J., Zaveri, R. A., Easter, R. C., Riemer, N., and Fast, J. D.: A three-dimensional sectional representation of aerosol mixing state for simulating optical properties and cloud condensation nuclei, *Journal of Geophysical Research: Atmospheres*, 121, 5912–5929, <https://doi.org/10.1002/2015JD024323>, 2016.
- Ching, J., Fast, J., West, M., and Riemer, N.: Metrics to quantify the importance of mixing state for CCN activity, *Atmos. Chem. Phys.*, 17, 7445–7458, <https://doi.org/10.5194/acp-17-7445-2017>, 2017.
- Ching, J., Adachi, K., Zaizen, Y., Igarashi, Y., and Kajino, M.: Aerosol mixing state revealed by transmission electron microscopy pertaining to cloud formation and human airway deposition, *npj Climate and Atmospheric Science*, 2, 22, <https://doi.org/10.1038/s41612-019-0081-9>, 2019.
- Collins, D. B., Ault, A. P., Moffet, R. C., Ruppel, M. J., Cuadra-Rodriguez, L. A., Guasco, T. L., Corrigan, C. E., Pedler, B. E., Azam, F., Aluwihare, L. I., Bertram, T. H., Roberts, G. C., Grassian, V. H., and Prather, K. A.: Impact of marine biogeochemistry on the chemical mixing state and cloud forming ability of nascent sea spray aerosol, *Journal of Geophysical Research: Atmospheres*, 118, 8553–8565, <https://doi.org/10.1002/jgrd.50598>, 2013.
- Cheung, H. C., Chou, C. C. K., Lee, C. S. L., Kuo, W. C., and Chang, S. C.: Hygroscopic properties and cloud condensation nuclei activity of atmospheric aerosols under the influences of Asian continental outflow and new particle formation at a coastal site in eastern Asia, *Atmos. Chem. Phys.*, 20, 5911–5922, <https://doi.org/10.5194/acp-20-5911-2020>, 2020.
- Cai, J., Chu, B., Yao, L., Yan, C., Heikkinen, L. M., Zheng, F., Li, C., Fan, X., Zhang, S., Yang, D., Wang, Y., Kokkonen, T. V., Chan, T., Zhou, Y., Dada, L., Liu, Y., He, H., Paasonen, P., Kujansuu, J. T., Petäjä, T., Mohr, C., Kangasluoma, J., Bianchi, F., Sun, Y., Croteau, P. L., Worsnop, D. R., Kerminen, V. M., Du, W., Kulmala, M., and Daellenbach, K. R.: Size-segregated particle number and mass concentrations from different emission sources in urban Beijing, *Atmos. Chem. Phys.*, 20, 12721–12740, <https://doi.org/10.5194/acp-20-12721-2020>, 2020.
- Dusek, U., Frank, G. P., Hildebrandt, L., Curtius, J., Schneider, J., Walter, S., Chand, D., Drewnick, F., Hings, S., Jung, D., Borrmann, S., and Andreae, M. O.: Size matters more than chemistry for cloud-nucleating ability of aerosol particles, *Science*, 312, 1375–1378, <https://doi.org/10.1126/science.1125261>, 2006.
- DeCarlo, P. F., Kimmel, J. R., Trimborn, A., Northway, M. J., Jayne, J. T., Aiken, A. C., Gonin, M., Fuhrer, K., Hor-

- vath, T., Docherty, K. S., Worsnop, D. R., and Jimenez, J. L.: Field-deployable, high-resolution, time-of-flight aerosol mass spectrometer, *Analytical Chemistry*, 78, 8281–8289, <https://doi.org/10.1021/ac061249n>, 2006.
- Ervens, B., Cubison, M. J., Andrews, E., Feingold, G., Ogren, J. A., Jimenez, J. L., Quinn, P. K., Bates, T. S., Wang, J., Zhang, Q., Coe, H., Flynn, M., and Allan, J. D.: CCN predictions using simplified assumptions of organic aerosol composition and mixing state: a synthesis from six different locations, *Atmos. Chem. Phys.*, 10, 4795–4807, <https://doi.org/10.5194/acp-10-4795-2010>, 2010.
- Fierce, L., Onasch, T. B., Cappa, C. D., Mazzoleni, C., China, S., Bhandari, J., Davidovits, P., Fischer, D. A., Helgestad, T., Lambe, A. T., Sedlacek, A. J., Smith, G. D., and Wolff, L.: Radiative absorption enhancements by black carbon controlled by particle-to-particle heterogeneity in composition, *P. Natl. Acad. Sci. USA*, 117, 5196–5203, <https://doi.org/10.1073/pnas.1919723117>, 2020.
- Fan, X., Liu, J., Zhang, F., Chen, L., Collins, D., Xu, W., Jin, X., Ren, J., Wang, Y., Wu, H., Li, S., Sun, Y., and Li, Z.: Contrasting size-resolved hygroscopicity of fine particles derived by HTDMA and HR-ToF-AMS measurements between summer and winter in Beijing: the impacts of aerosol aging and local emissions, *Atmos. Chem. Phys.*, 20, 915–929, <https://doi.org/10.5194/acp-20-915-2020>, 2020.
- Gysel, M., McFiggans, G. B., and Coe, H.: Inversion of tandem differential mobility analyser (TDMA) measurements, *Journal of Aerosol Science*, 40, 134–151, <https://doi.org/10.1016/j.jaerosci.2008.07.013>, 2009.
- Hughes, M., Kodros, J. K., Pierce, J. R., West, M., and Riemer, N.: Machine learning to predict the global distribution of aerosol mixing state metrics, *Atmosphere*, 9, 15, <https://doi.org/10.3390/atmos9010015>, 2018.
- Huang, R. J., Zhang, Y., Bozzetti, C., Ho, K. F., Cao, J. J., Han, Y., Daellenbach, K. R., Slowik, J. G., Platt, S. M., Canonaco, F., Zotter, P., Wolf, R., Pieber, S. M., Bruns, E. A., Crippa, M., Ciarelli, G., Piazzalunga, A., Schwikowski, M., Abbaszade, G., Schnelle-Kreis, J., Zimmermann, R., An, Z., Szidat, S., Baltensperger, U., Haddad, I. E., and Prévôt, A. S.: High secondary aerosol contribution to particulate pollution during haze events in China, *Nature*, 514, 218–222, <https://doi.org/10.1038/nature13774>, 2014.
- IPCC (Intergovernmental Panel on Climate Change): Climate Change 2021: The Physical Science Basis. Contribution of Working Group I to the Sixth Assessment Report of the Intergovernmental Panel on Climate Change, edited by: Masson-Delmotte, V., Zhai, P., Pirani, A., Connors, S. L., Péan, C., Berger, S., Caud, N., Chen, Y., Goldfarb, L., Gomis, M. I., Huang, M., Leitzell, K., Lonnoy, E., Matthews, J. B. R., Maycock, T. K., Waterfield, T., Yelekçi, O., Yu, R., and Zhou, B., Cambridge University Press, Cambridge, United Kingdom and New York, NY, USA, 2391 pp., <https://doi.org/10.1017/9781009157896>, 2021.
- Liu, P., Song, M., Zhao, T., Gunthe, S. S., Ham, S., He, Y., Qin, Y., Gong, Z., Amorim, C. J., Bertram, K. A., and Martin, S. T.: Resolving the mechanisms of hygroscopic growth and cloud condensation nuclei activity for organic particulate matter, *Nature Communications*, 9, 4076, <https://doi.org/10.1038/s41467-018-06622-2>, 2018.
- Liu, J., Zhang, F., Ren, J., Chen, L., Zhang, A., Wang, Z., Zou, S., Xu, H., and Yue, X.: The evolution of aerosol mixing state derived from a field campaign in Beijing: implications for particle aging timescales in urban atmospheres, *Atmos. Chem. Phys.*, 25, 5075–5086, <https://doi.org/10.5194/acp-25-5075-2025>, 2025.
- Liu, Y., Lin, T., Zhang, J., Wang, F., Huang, Y., Wu, X., Ye, H., Zhang, G., Cao, X., and de Leeuw, G.: Opposite effects of aerosols and meteorological parameters on warm clouds in two contrasting regions over eastern China, *Atmos. Chem. Phys.*, 24, 4651–4673, <https://doi.org/10.5194/acp-24-4651-2024>, 2024.
- Lance, S., Nenes, A., Medina, J., and Smith, J. N.: Mapping the operation of the DMT continuous flow CCN counter, *Aerosol Science and Technology*, 40, 242–254, <https://doi.org/10.1080/02786820500543290>, 2006.
- Manavi, S. E. I., Aktypis, A., Siouti, E., Skyllakou, K., Myriokefalitakis, S., Kanakidou, M., and Pandis, S. N.: Atmospheric aerosol spatial variability: Impacts on air quality and climate change, *One Earth*, 8, <https://doi.org/10.1016/j.oneear.2025.101237>, 2025.
- Ovadnevaite, J., Ceburnis, D., Leinert, S., Dall’Osto, M., Canagaratna, M., O’Doherty, S., Berresheim, H., and O’Dowd, C.: Submicron NE Atlantic marine aerosol chemical composition and abundance: Seasonal trends and air mass categorization, *Journal of Geophysical Research: Atmospheres*, 119, 11850–11863, <https://doi.org/10.1002/2013JD021330>, 2014.
- Petters, M. D. and Kreidenweis, S. M.: A single parameter representation of hygroscopic growth and cloud condensation nucleus activity, *Atmos. Chem. Phys.*, 7, 1961–1971, <https://doi.org/10.5194/acp-7-1961-2007>, 2007.
- Padró, L. T., Moore, R. H., Zhang, X., Rastogi, N., Weber, R. J., and Nenes, A.: Mixing state and compositional effects on CCN activity and droplet growth kinetics of size-resolved CCN in an urban environment, *Atmos. Chem. Phys.*, 2012, 10239–10255, <https://doi.org/10.5194/acp-12-10239-2012>, 2012.
- Ramachandran, S. and Srivastava, R.: Mixing states of aerosols over four environmentally distinct atmospheric regimes in Asia: coastal, urban, and industrial locations influenced by dust, *Environmental Science and Pollution Research*, 23, 11109–11128, <https://doi.org/10.1007/s11356-016-6254-8>, 2016.
- Ren, J., Zhang, F., Wang, Y., Collins, D., Fan, X., Jin, X., Xu, W., Sun, Y., Cribb, M., and Li, Z.: Using different assumptions of aerosol mixing state and chemical composition to predict CCN concentrations based on field measurements in urban Beijing, *Atmos. Chem. Phys.*, 18, 6907–6921, <https://doi.org/10.5194/acp-18-6907-2018>, 2018.
- Ren, J., Zhang, F., Chen, L., Cao, G., Liu, M., Li, X., Wu, H., Cheng, Y., and Li, Z.: Identifying the hygroscopic properties of fine aerosol particles from diverse sources in urban atmosphere and the applicability in prediction of cloud nuclei, *Atmos. Environ.*, 298, 119615, <https://doi.org/10.1016/j.atmosenv.2023.119615>, 2023.
- Riemer, N. and West, M.: Quantifying aerosol mixing state with entropy and diversity measures, *Atmos. Chem. Phys.*, 13, 11423–11439, <https://doi.org/10.5194/acp-13-11423-2013>, 2013.
- Riemer, N., Ault, A. P., West, M., Craig, R. L., and Curtis, J. H.: Aerosol mixing state: Measurements, modeling, and impacts, *Reviews of Geophysics*, 57, 187–249, <https://doi.org/10.1029/2018RG000615>, 2019.

- Rose, D., Gunthe, S. S., Mikhailov, E., Frank, G. P., Dusek, U., Andreae, M. O., and Pöschl, U.: Calibration and measurement uncertainties of a continuous-flow cloud condensation nuclei counter (DMT-CCNC): CCN activation of ammonium sulfate and sodium chloride aerosol particles in theory and experiment, *Atmos. Chem. Phys.*, 8, 1153–1179, <https://doi.org/10.5194/acp-8-1153-2008>, 2008.
- Rosenfeld, D., Zhu, Y., Wang, M., Zheng, Y., Goren, T., and Yu, S.: Aerosol – driven droplet concentrations dominate coverage and water of oceanic low-level clouds, *Science*, 363, 6427, <https://doi.org/10.1126/science.aay4194>, 2019.
- Schill, S. R., Collins, D. B., Lee, C., Morris, H. S., Novak, G. A., Prather, K. A., Quinn, P. K., Sultana, C. M., Tivanski, A. V., Zimmermann, K., Cappa, C. D., and Bertram, T. H.: The impact of aerosol particle mixing state on the hygroscopicity of sea spray aerosol, *ACS Central Science*, 1, 132–141, <https://doi.org/10.1021/acscentsci.5b00174>, 2015.
- Shi, Z., Vu, T., Kotthaus, S., Harrison, R. M., Grimmond, S., Yue, S., Zhu, T., Lee, J., Han, Y., Demuzere, M., Dunmore, R. E., Ren, L., Liu, D., Wang, Y., Wild, O., Allan, J., Acton, W. J., Barlow, J., Barratt, B., Beddows, D., Bloss, W. J., Calzolari, G., Carruthers, D., Carslaw, D. C., Chan, Q., Chatzidiakou, L., Chen, Y., Crilley, L., Coe, H., Dai, T., Doherty, R., Duan, F., Fu, P., Ge, B., Ge, M., Guan, D., Hamilton, J. F., He, K., Heal, M., Heard, D., Hewitt, C. N., Hollaway, M., Hu, M., Ji, D., Jiang, X., Jones, R., Kalberer, M., Kelly, F. J., Kramer, L., Langford, B., Lin, C., Lewis, A. C., Li, J., Li, W., Liu, H., Liu, J., Loh, M., Lu, K., Lucarelli, F., Mann, G., McFiggans, G., Miller, M. R., Mills, G., Monk, P., Nemitz, E., O'Connor, F., Ouyang, B., Palmer, P. I., Percival, C., Popoola, O., Reeves, C., Rickard, A. R., Shao, L., Shi, G., Spracklen, D., Stevenson, D., Sun, Y., Sun, Z., Tao, S., Tong, S., Wang, Q., Wang, W., Wang, X., Wang, X., Wang, Z., Wei, L., Whalley, L., Wu, X., Wu, Z., Xie, P., Yang, F., Zhang, Q., Zhang, Y., Zhang, Y., and Zheng, M.: Introduction to the special issue “In-depth study of air pollution sources and processes within Beijing and its surrounding region (APHH-Beijing)”, *Atmos. Chem. Phys.*, 19, 7519–7546, <https://doi.org/10.5194/acp-19-7519-2019>, 2019.
- Shrivastava, M., Cappa, C. D., Fan, J., Goldstein, A. H., Guenther, A. B., Jimenez, J. L., Kuang, C., Laskin, A., Martin, S. T., Ng, N. L., Petaja, T., Pierce, J. R., Rasch, P. J., Roldin, P., Seinfeld, J. H., Shilling, J., Smith, J. N., Thornton, J. A., Volkamer, R., Wang, J., Worsnop, D. R., Zaveri, R. A., Zelenyuk, A., and Zhang, Q.: Recent advances in understanding secondary organic aerosol: Implications for global climate forcing, *Reviews of Geophysics*, 55, 509–559, <https://doi.org/10.1002/2016RG000540>, 2017.
- Sotiropoulou, R. E. P., Nenes, A., Adams, P. J., and Seinfeld, J. H.: Cloud condensation nuclei prediction error from application of Köhler theory: Importance for the aerosol indirect effect, *Journal of Geophysical Research: Atmospheres*, 112, <https://doi.org/10.1029/2006JD007834>, 2007.
- Spitieri, C., Gini, M., Gysel-Beer, M., and Eleftheriadis, K.: Annual cycle of hygroscopic properties and mixing state of the suburban aerosol in Athens, Greece, *Atmos. Chem. Phys.*, 23, 235–249, <https://doi.org/10.5194/acp-23-235-2023>, 2023.
- Stevens, R. and Dastoor, A.: A Review of the Representation of Aerosol Mixing State in Atmospheric Models, *Atmosphere*, 10, 168, <https://doi.org/10.3390/atmos10040168>, 2019.
- Stokes, R. H. and Robinson, R. A.: Interactions in aqueous nonelectrolyte solutions, I. Solute-Solvent equilibria, *Journal of Physical Chemistry*, 70, 2126–2130, <https://doi.org/10.1021/j100879a010>, 1966.
- Tao, J., Kuang, Y., Ma, N., Hong, J., Sun, Y., Xu, W., Zhang, Y., He, Y., Luo, Q., Xie, L., Su, H., and Cheng, Y.: Secondary aerosol formation alters CCN activity in the North China Plain, *Atmos. Chem. Phys.*, 21, 7409–7427, <https://doi.org/10.5194/acp-21-7409-2021>, 2021.
- Tao, J., Luo, B., Xu, W., Zhao, G., Xu, H., Xue, B., Zhai, M., Xu, W., Zhao, H., Ren, S., Zhou, G., Liu, L., Kuang, Y., and Sun, Y.: Markedly different impacts of primary emissions and secondary aerosol formation on aerosol mixing states revealed by simultaneous measurements of CCNC, H(V)/TDMA, and SP2, *Atmos. Chem. Phys.*, 24, 9131–9154, <https://doi.org/10.5194/acp-24-9131-2024>, 2024.
- Virtanen, A., Joutsensaari, J., Kokkola, H., Partridge, G. D., Blichner, S., Seland, Ø., Holopainen, E., Tovazzi, E., Lipponen, A., Mikkonen, S., Leskinen, A., Hyvärinen, A., Zieger, P., Krejci, R., Ekman, A. M. L., Riipinen, I., Quaas, J., and Romakkaniemi, S.: High sensitivity of cloud formation to aerosol changes, *Nature Geoscience*, 18, 289–295, <https://doi.org/10.1038/s41561-025-01662-y>, 2025.
- Winkler, P.: The growth of atmospheric aerosol particles as a function of the relative humidity – II. An improved concept of mixed nuclei, *Journal of Aerosol Science*, 4, 373–387, [https://doi.org/10.1016/0021-8502\(73\)90027-X](https://doi.org/10.1016/0021-8502(73)90027-X), 1973.
- Wang, J., Cubison, M. J., Aiken, A. C., Jimenez, J. L., and Collins, D. R.: The importance of aerosol mixing state and size-resolved composition on CCN concentration and the variation of the importance with atmospheric aging of aerosols, *Atmos. Chem. Phys.*, 10, 7267–7283, <https://doi.org/10.5194/acp-10-7267-2010>, 2010.
- Wang, Y., Li, Z., Zhang, R., Jin, X., Xu, W., Fan, X., Wu, H., Zhang, F., Sun, Y., Wang, Q., Cribb, M., and Hu, D.: Distinct ultrafine- and accumulation-mode particle properties in clean and polluted urban environments, *Geophysical Research Letters*, 46, 10918–10925, <https://doi.org/10.1029/2019GL084047>, 2019.
- Xie, C., He, Y., Lei, L., Zhou, W., Liu, J., Wang, Q., Xu, W., Qiu, Y., Zhao, J., Sun, J., Li, L., Li, M., Zhou, Z., Fu, P., Wang, Z., and Sun, Y.: Contrasting mixing state of black carbon-containing particles in summer and winter in Beijing, *Environ. Pollution*, 263, 114455, <https://doi.org/10.1016/j.envpol.2020.114455>, 2020.
- Xu, W., Sun, Y., Wang, Q., Zhao, J., Wang, J., Ge, X., Xie, C., Zhou, W., Du, W., Li, J., Fu, P., Wang, Z., Worsnop, D. R., and Coe, H.: Changes in aerosol chemistry from 2014 to 2016 in winter in Beijing: Insights from high-resolution aerosol mass spectrometry, *Journal of Geophysical Research: Atmospheres*, 124, 1132–1147, <https://doi.org/10.1029/2018JD029245>, 2019.
- Xu, W., Ovadnevaite, J., Fossom, K. N., Lin, C., Huang, R. J., O'Dowd, C., and Ceburnis, D.: Aerosol hygroscopicity and its link to chemical composition in the coastal atmosphere of Mace Head: marine and continental air masses, *Atmos. Chem. Phys.*, 20, 3777–3791, <https://doi.org/10.5194/acp-20-3777-2020>, 2020.
- Xu, W., Ovadnevaite, J., Fossom, K. N., Lin, C., Huang, R. J., O'Dowd, C., and Ceburnis, D.: Seasonal trends of aerosol hygroscopicity and mixing state in clean marine and polluted continental air masses over the Northeast Atlantic, *Journal*

- of Geophysical Research: Atmospheres, 126, e2020JD033851, <https://doi.org/10.1029/2020JD033851>, 2021a.
- Xu, W., Fossum, K. N., Ovadnevaite, J., Lin, C., Huang, R. J., O'Dowd, C., and Ceburnis, D.: The impact of aerosol size-dependent hygroscopicity and mixing state on the cloud condensation nuclei potential over the north-east Atlantic, *Atmos. Chem. Phys.*, 21, 8655–8675, <https://doi.org/10.5194/acp-21-8655-2021>, 2021b.
- Xu, W., Ovadnevaite, J., Fossum, K. N., Lin, C., Huang, R. J., Ceburnis, D., and O'Dowd, C.: Sea spray as an obscured source for marine cloud nuclei, *Nature Geoscience*, 15, 282–286, <https://doi.org/10.1038/s41561-022-00917-2>, 2022.
- Xu, W., Ovadnevaite, J., Fossum, K. N., Huang, R. J., Huang, D., Zhong, H., Gu, Y., Lin, C., Huang, C., O'Dowd, C., and Ceburnis, D.: Condensation of organic-inorganic vapours governs the production of ultrafine secondary marine cloud nuclei, *Communications Earth and Environment*, 5, 359, <https://doi.org/10.1038/s43247-024-01519-z>, 2024.
- Yang, F., Chen, H., Du, J., Yang, X., Gao, S., Chen, J., and Geng, F.: Evolution of the mixing state of fine aerosols during haze events in Shanghai, *Atmospheric Research*, 104, 193–201, <https://doi.org/10.1016/j.atmosres.2011.10.005>, 2012.
- Ye, Q., Gu, P., Li, H. Z., Robinson, E. S., Lipsky, E. M., Kaltsounoudis, C., Lee, A. K. Y., Apte, J. S., Robinson, A. L., Sullivan, R. C., Presto, A. A., and Donahue, N. M.: Spatial variability of sources and mixing state of atmospheric particles in a metropolitan area, *Environmental Science and Technology*, 52, 6807–6815, <https://doi.org/10.1021/acs.est.8b01011>, 2018.
- Yuan, L. and Zhao, C.: Quantifying particle-to-particle heterogeneity in aerosol hygroscopicity, *Atmos. Chem. Phys.*, 23, 3195–3205, <https://doi.org/10.5194/acp-23-3195-2023>, 2023.
- Zdanovskii, A.: New methods for calculating solubilities of electrolytes in multicomponent systems, *Zh. Fiz. Khim. C*, 22, 1475–1485, 1948.
- Zhao, G., Tan, T., Zhu, Y., Hu, M., and Zhao, C.: Method to quantify black carbon aerosol light absorption enhancement with a mixing state index, *Atmos. Chem. Phys.*, 21, 18055–18063, <https://doi.org/10.5194/acp-21-18055-2021>, 2021.
- Zheng, Z., Curtis, J. H., Yao, Y., Gasparik, J. T., Anantharaj, V. G., Zhao, L., West, M., and Riemer, N.: Estimating submicron aerosol mixing state at the global scale with machine learning and Earth system modeling, *Earth and Space Science*, 8, e2020EA001500, <https://doi.org/10.1029/2020EA001500>, 2021a.
- Zheng, Z., West, M., Zhao, L., Ma, P.-L., Liu, X., and Riemer, N.: Quantifying the structural uncertainty of the aerosol mixing state representation in a modal model, *Atmos. Chem. Phys.*, 21, 17727–17741, <https://doi.org/10.5194/acp-21-17727-2021>, 2021b.
- Zhong, H., Huang, R. J., Lin, C., Xu, W., Duan, J., Gu, Y., Huang, W., Ni, H.; Zhu, C., You, Y., Wu, Y., Zhang, R., Ovadnevaite, J., Ceburnis, D., and O'Dowd, C.: Measurement report: On the contribution of long-distance transport to the secondary aerosol formation and aging, *Atmos. Chem. Phys.*, 22, 9513–9524, <https://doi.org/10.5194/acp-22-9513-2022>, 2022.